ACS APPLIED MATERIALS & INTERFACES

Research Article

www.acsami.org

Asymmetric Paper Supercapacitor Based on Amorphous Porous Mn_3O_4 Negative Electrode and $Ni(OH)_2$ Positive Electrode: A Novel and High-Performance Flexible Electrochemical Energy Storage Device

Jin-Xian Feng, Sheng-Hua Ye, Xue-Feng Lu, Ye-Xiang Tong, and Gao-Ren Li*

MOE Laboratory of Bioinorganic and Synthetic Chemistry, KLGHEI of Environment and Energy Chemistry, School of Chemistry and Chemical Engineering, Sun Yat-Sen University, No. 135 Xinguang Road, Guangzhou 510275, China

Supporting Information

ABSTRACT: Here we synthesize novel asymmetric all-solid-state paper supercapacitors (APSCs) based on amorphous porous Mn_3O_4 grown on conducting paper (NGP) (Mn_3O_4/NGP) negative electrode and $Ni(OH)_2$ grown on NGP ($Ni(OH)_2$/NGP) as positive electrode, and they have attracted intensive research interest owing to their outstanding properties such as being flexible, ultrathin, and lightweight. The fabricated APSCs exhibit a high areal C_{sp} of 3.05 F/cm^3 and superior cycling stability. The novel asymmetric APSCs also exhibit high energy density of 0.35 mW h/cm^3, high power density of 32.5 mW/cm^3, and superior cycling performance (<17% capacitance loss after 12 000 cycles at a high scan rate of 100 mV/s). This work shows the first example of amorphous porous metal oxide/NGP electrodes for the asymmetric APSCs, and these systems hold great potential for future flexible electronic devices.

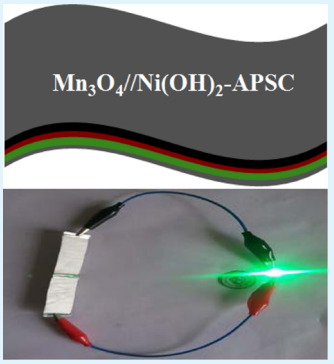

KEYWORDS: *asymmetric supercapacitor, paper-based, amorphous Mn_3O_4, negative electrode, flexible, porous structure*

1. INTRODUCTION

Flexible and portable electronics is a rapidly emerging technology, and great progress has been obtained such as wearable/rollup displays, artificial electronic skin, hand-held portable devices, and sensor networks. The rapid development of flexible and portable electronics has promoted the needs for flexible and lightweight energy sources with high power, high energy, and a long cycle life.[1−14] As some of the most promising energy storage devices, all-solid-state paper supercapacitors (APSCs) have attracted intensive research interest owing to their outstanding properties such as flexibility, ultrathin thickness, high power density, and light weight, which enable great promise in the field of flexible and portable electronics.[15−17] The APSCs will enable the entire device to be thin, flexible, and possibly compact. However, to meet the increasing energy demands for next-generation electronic devices, the energy density of APSCs must be boosted further within confined volume or footprint areas.[18,19]

In order to overcome the energy density limit of APSCs, one effective strategy is to construct asymmetric supercapacitors (ASCs) that can operate in much wider potential windows and may lead to a substantial increase in the energy density of device.[20−23] The design of the asymmetric APSCs with high performance is highly attractive for flexible and portable electronics. In the ASC device, a battery-type Faradaic electrode (positive electrode) plays the energy source role and a capacitor-type electrode (negative electrode) plays as the power source role. The positive electrode can consist of a lot of materials, such as NiO, MnO_2, V_2O_5, etc.[24−27] Despite of the great progress of positive electrode materials, the negative electrode materials for ASCs still lack full consideration.[28] So far, carbon materials, such as active carbon, carbon nanotubes, and graphene, have been widely used as negative electrode for ASCs because of their excellent electrical conductivity, large surface area, and outstanding electrochemical stability.[29−31] However, the carbon materials usually suffer from harsh producing processes and relative low capacitance (100−300 F/g). In order to further improve the performance of negative electrode of ASCs, some new materials, such as Fe_2O_3,[28] MoO_{3-x},[32] and Co_9S_8,[33] have been developed. However, the electrochemical performances of the most recently reported negative electrodes are limited due to their low capacitance and poor cycle ability.

In this work, we developed a novel asymmetric paper-based supercapacitor based on Mn_3O_4 and $Ni(OH)_2$ grown on conducting paper (Ni/graphite/paper, NGP) as negative and positive electrodes, respectively, for APSCs (denoted as Mn_3O_4//$Ni(OH)_2$-APSCs). The negative electrode for the APSCs, Mn_3O_4, whose structure is $Mn(II)[Mn(III)]_2O_4$, has +2 and +3 valences for element Mn,[32] so the element Mn has

Received: March 11, 2015
Accepted: May 11, 2015
Published: May 11, 2015

ACS Publications © 2015 American Chemical Society

DOI: 10.1021/acsami.5b02157
ACS Appl. Mater. Interfaces 2015, 7, 11444−11451

multiple valences and it can provide rich redox reactions for pseudocapacitance generation. What's more, Mn_3O_4 has a suitable working window in the negative potential (−0.8−0 V) and is low cost, highly abundant, and nontoxic. The amorphous porous Mn_3O_4 grown on NGP (Mn_3O_4/NGP) has excellent flexibility. The design of such amorphous porous Mn_3O_4/NGP exhibits the following aims: (i) The amorphous porous Mn_3O_4/NGP will relax ion transport because of the short ion diffusion paths and can provide reversible and fast faradic reactions. (ii) The porous structure will improve the utilization rates of electrode materials because of the areal surface enhancement. The amorphous porous Mn_3O_4 will let each Mn_3O_4 nanosheet available take part in electrochemical reactions because of the full contact between electrolyte and Mn_3O_4. (iii) Because the Mn_3O_4 layer attaches tightly with the Ni layer, this will help overcome the limited electric conductivity of Mn_3O_4. The results in this study prove that the fabricated amorphous porous Mn_3O_4/NGP exhibits high C_{sp}, superior rate capability, and great long-term cycle life, and is a potential electrode material for SCs with high performance. The amorphous porous Mn_3O_4/NGP exhibits high areal specific capacitance (C_{sp}) of 432 mF/cm^2 and superior cycling stability. The positive electrode for the APSCs is $Ni(OH)_2$/NGP, which is also amorphous and flexible. The C_{sp} of $Ni(OH)_2$/NGP can reach as high as 1646 mF/cm^2 at 5 mV/s. The assembled flexible Mn_3O_4//$Ni(OH)_2$-APSCs exhibit large volumetric C_{sp} of 3.05 F/cm^3, superior cycling stability (<17% C_{sp} loss after 12 000 cycles at a high scan rate of 100 mV/s), and high energy/power densities (0.35 mW h/cm^3, 32.5 mW/cm^3).

2. EXPERIMENTAL SECTION

Fabrication of NGP. The normal cellulose paper was purchased from the supermarket in Sun Yat-Sen University in Guangzhou, China. The homogeneous graphite layer on paper was first fabricated by the following procedures: the graphite powder was first sprayed on the surface of paper (amount of powder: 1 mg/cm^2) and "pushed" onto paper by using the force of ∼15 N/cm^2. Then, a uniform graphite layer on paper (namely, graphite/paper) was obtained by drawing a graphite rod (spectrum grade) to and fro many times. A homogeneous Ni layer was then fabricated on the graphite/paper (namely, Ni/graphite/paper, NGP) by galvanostatic electrodeposition in a conventional three-electrode glass cell at 20 °C for 15 min. The counter electrode is a Ni plate (99.9%, 2.0 cm^2), and the saturated calomel electrode (SCE) was used as reference electrode that was connected to the cell with a double salt bridge system. The current density of electrodeposition is 5 mA/cm^2. The deposition solution is 0.1 M $NiSO_4 \cdot 6H_2O$ + 0.1 M $NiCl_2 \cdot 6H_2O$ + 0.5 M H_3BO_3 + 3.47 × 10^{-5} M sodium dodecyl sulfate, and the pH value is 3−4. The fabricated NGP was placed in an autoclave oven at 100 °C for 180 min to remove the excessive moisture.

Preparation of Amorphous Porous Mn_3O_4/NGP. Amorphous porous Mn_3O_4 was fabricated via electrodeposition method with current density of 1.0 mA/cm^2 in a solution of 0.05 M $MnAc_2$ + 0.1 M KAc + dimethyl sulfoxide (10%) at 70 °C for 30 min. A uniform yellow-brown layer of amorphous porous Mn_3O_4 nanosheets was coated on the NGP and washed with deionized water. To remove the excessive moisture, the as-prepared Mn_3O_4 samples were thermally annealed at 120 °C in air. The mass of Mn_3O_4 was obtained using electronic scales (BT25S, 0.01 mg).

Preparation of $Ni(OH)_2$/NGP. $Ni(OH)_2$ was prepared on NGP by anodic electrodoxidation using a Hull cell texter (Technology Institute of Guangzhou second Light Industry). The electrodoxidation was conducted in a solution containing sodium nitrate (0.1 M, 17 mL) at 1.0 V for 10 min at room temperature and heated at 100 °C for 15 min.

Assembling of Flexible and Asymmetric APSCs. The flexible and asymmetric Mn_3O_4//$Ni(OH)_2$-APSCs were assembled by using the amorphous porous Mn_3O_4/NGP as negative electrode and amorphous $Ni(OH)_2$/NGP as positive electrode. The amorphous porous Mn_3O_4/NGP electrode and amorphous $Ni(OH)_2$/NGP electrode were separated with a separator (filter paper, Shuangquan Brand, Hangzhou Paper Corporation). The poly(vinyl alcohol) (PVA)/NaOH gel was used as the electrolyte. The PVA/NaOH gel was prepared by mixing NaOH (1.0 M, 30 mL) and PVA (2.0 g) and heated at 80 °C for 1 h under vigorous stirring. Prior to assembly, the electrodes and separator were soaked in the PVA/NaOH solution, and then the gel was allowed to solidify around them at room temperature for 6 h. Finally, they were assembled together and heated at 35 °C for 12 h to remove excess water in the electrolyte.

Material Characterizations and Electrochemical Measurements. The morphology, structure, and composition of electrode materials were characterized by field emission SEM (FE-SEM, JSM-6330F), TEM (TEM, JEM2010-HR, 200 kV), and XPS (XPS, ESCA Lab 250, Thermo VG). All electrochemical measurements were conducted using an electrochemical workstation (CHI760D). The electrochemical studies of individual electrodes were performed in a three-electrode cell, with a Pt counter electrode and an SCE reference electrode, in 1 M NaOH aqueous solution. The capacitance of cycle votammertry was calculated as eqs 1 and 2 as follows:

$$C_{sp} = \frac{S}{2\nu \times \Delta U \times A} \ (\mathrm{F/cm^2}) \tag{1}$$

$$C_{sp} = \frac{S}{2\nu \times \Delta U \times m \times A} \ (\mathrm{F/g}) \tag{2}$$

Here C_{sp} is an areal capacitance (F/cm^2), S is the area enclosed by CV curve within the potential window, ΔU is the potential window (V), ν is the scan rate (mV/s), A is electrode area (cm^2), m is the loading mass (g), and the specific capacitance is based on mass (F/g).

The capacitance of galvanostatic charge−discharge was calculated as eqs 3 and 4 as follows:

$$C_{sp} = \frac{jt}{\Delta U} \ (\mathrm{F/cm^2}) \tag{3}$$

$$C_{sp} = \frac{jt}{\Delta U \times m} \ (\mathrm{F/g}) \tag{4}$$

Here C_{sp} is areal capacitance (F/cm^2), ΔU is the potential window (V), j the current density (A/cm^2), m is the loading mass (g), and the specific capacitance is based on mass (F/g).

The energy density (E) and power density (P) were calculated from the chronopotentiometric curves according to eqs 5 and 6:

$$E = \frac{C_{sp} \times (\Delta U)^2}{7200 \times V} \ (\mathrm{Wh/cm^3}) \tag{5}$$

$$P = \frac{E \times 3600}{\Delta t} (\mathrm{W/cm^3}) \tag{6}$$

Here C_{sp} is areal capacitance (F/cm^2), ΔU is the potential window (V), V is the volume of ATFSC device (cm^3), and Δt is discharge time (s).

3. RESULTS AND DISCUSSION

The details of the fabrication of NGP are described in the Experimental Section and in Supporting Information. To fabricate a Mn_3O_4/NGP electrode, the amorphous porous Mn_3O_4 was directly electrodeposited on NGP as illustrated in Figure 1a. The SEM image of the surface of NGP before electrodeposition is shown in Figure 1b, which shows that the surface of NGP is smooth. After electrodeposition of Mn_3O_4, a black film was uniformly covered on NGP, and the SEM image shows that the Mn_3O_4 film is a porous structure as shown in Figure 1c. The thickness of a Mn_3O_4 film is ∼1.0 μm. HRTEM

DOI: 10.1021/acsami.5b02157
ACS Appl. Mater. Interfaces 2015, 7, 11444−11451

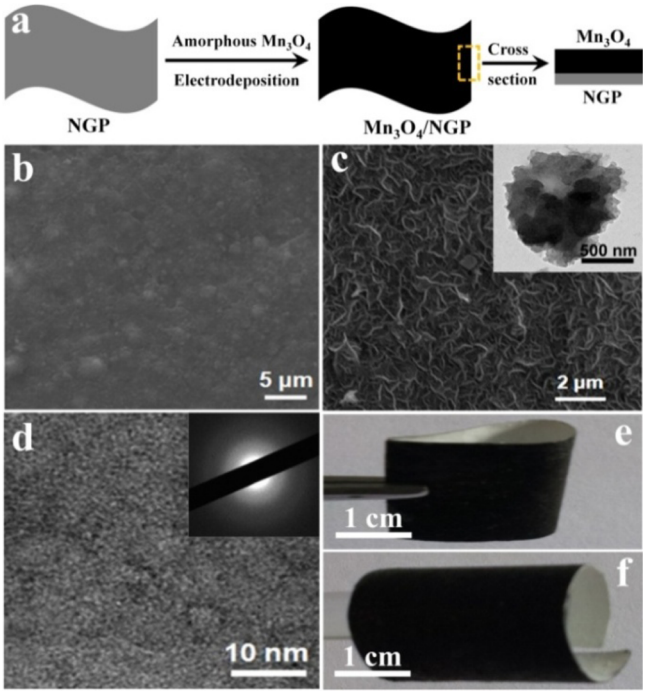

Figure 1. (a) Schematic illustration for the fabrication of Mn_3O_4/NGP electrode, (b) SEM image of surface morphology of NGP, (c) SEM image of surface morphology of Mn_3O_4/NGP electrode (inset shows TEM image of Mn_3O_4 nanosheet), (d) HRTEM image and SAED pattern of Mn_3O_4 nanosheet, and (e, f) optical images of Mn_3O_4/NGP electrode with excellent flexibility.

image and SAED pattern reveal that the Mn_3O_4 film is amorphous as shown in Figure 1d. The fabricated amorphous porous Mn_3O_4/NGP electrodes own excellent flexibility as shown in the optical images in Figure 1e,f.

The XRD pattern of the amorphous porous Mn_3O_4/NGP is shown in Figure 2a. Besides the peaks of NGP, no other peak is seen, and this result further proves that the Mn_3O_4 film is amorphous. X-ray photoelectron spectroscopy (XPS) measurement was performed to study the composition and oxidation state of amorphous porous Mn_3O_4. The XPS spectra collected from the amorphous porous Mn_3O_4 samples confirm the presence of Mn and O. The mutiplet splitting Mn 3s peaks are

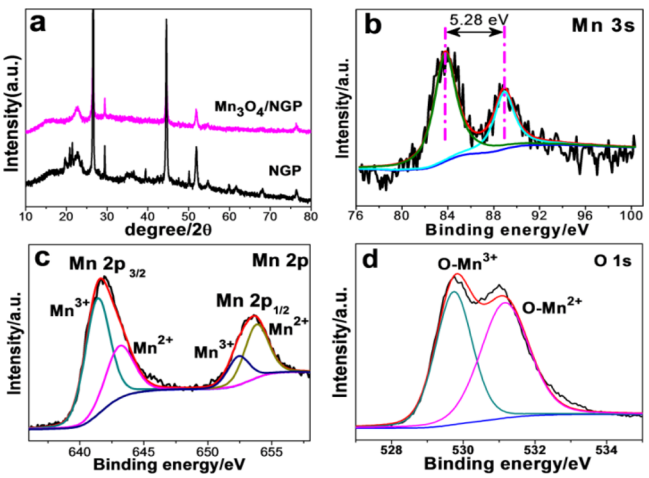

Figure 2. (a) XRD patterns of Mn_3O_4/NGP and NGP. XPS spectra of (b) Mn 3s, (c) Mn 2p, and (d) O 1s of Mn_3O_4/NGP.

useful for determining the oxidation state of Mn, and high-resolution XPS spectrum of Mn 3s is shown in Figure 2b. The binding energy separation of Mn 3s peaks is ~5.28 eV, which is consistent with that of Mn_3O_4 reported before (~5.3 eV).[35−37] Additionally, Figure 2c presents Mn $2p_{3/2}$ and $2p_{1/2}$ peaks of Mn_3O_4, and they both can be deconvoluted into two pairs of doublets. The peaks centered at 641.7 and 653.5 eV and those centered at 645.4 and 655.5 eV can be well-assigned to Mn^{3+} and Mn^{2+}, respectively.[35,36] The high-resolution O 1s spectrum is shown in Figure 2d, which shows the O 1s spectrum can be deconvoluted into two components, suggesting the presence of two kinds of oxygen-containing species. The O peak centered at 529.7 eV is attributed to the lattice oxygen of amorphous O−Mn^{3+}, while the O peak located at 530.9 eV corresponds to the lattice oxygen of O−Mn^{2+}.[38−40] In addition, EDS analysis shows that the atom ratio of Mn and O is 3:4. Therefore, the above results confirm well that the Mn_3O_4/NGP with multiple valences of Mn^{2+} and Mn^{3+} is successfully fabricated. The amorphous porous Mn_3O_4 exhibits a high BET specific surface area of about 60.23 m^2/g, and the relative details are shown in Supporting Information Figure S22.

Electrochemical properties of the amorphous porous Mn_3O_4/NGP were studied in a three-electrode cell in 1.0 M NaOH aqueous electrolyte. The cyclic voltammograms (CVs) of amorphous Mn_3O_4/NGP, crystalline Mn_3O_4/NGP, and bare NGP at the same scan rate (100 mV/s) are shown in Figure 3a, which shows that amorphous porous Mn_3O_4/NGP has much enhanced supercapacitive performance compared with that of the crystalline Mn_3O_4/NGP and bare NGP; the capacitive contribution of NGP is negligible. In order to illustrate the reversible ability of redox reactions in the amorphous porous Mn_3O_4/NGP electrodes, the di/dV−potential curves are measured and shown in Figure 3b. As shown in Figure 3b, either of the curves for positive or negative scan shows a peak current appearing at about −0.2 V versus SCE, and these two curves are symmetric to the x axis. This result shows that the amorphous porous Mn_3O_4/NGP electrodes have excellent reversibility of redox reactions. CVs of amorphous porous Mn_3O_4/NGP at various scan rates remain similar to scan rate increasing from 5 to 100 mV/s as shown in Supporting Information Figure S1, which further demonstrates good capacitive property and continuous fast and reversible redox reactions taking place in the amorphous porous Mn_3O_4. The areal specific capacitance (C_{sp}) at 5−100 mV/s and rate capability of the amorphous porous Mn_3O_4/NGP are shown in Figure 3c. The areal C_{sp} of amorphous porous Mn_3O_4/NGP electrode at 5 mV/s is 432 mF/cm^2 and the mass C_{sp} is 432 F/g (Mn_3O_4 loading is 1.0 mg/cm^2). The amorphous porous Mn_3O_4/NGP electrode shows much larger areal capacitances than the crystalline Mn_3O_4/NGP at the different scan rates as shown in Figure 3c. The C_{sp} of amorphous porous Mn_3O_4/NGP is also higher than those obtained for the various carbon negative electrodes, such as active carbon (30−250 F/g),[41,42] graphene (50−250 F/g),[43] and carbon nanotubes (30−150 F/g),[44] and they are also higher than many other metal oxide negative electrodes, such as α-Fe_2O_3 (100−300 mF/cm^2)[34] and α-MoO_3 (60−300 $\mu F/cm^2$)[47] at the same scan rate. Galvanostatic charging/discharging curves of amorphous porous Mn_3O_4/NGP at different current densities are shown in Figure 3d, and they all are symmetrical. This confirms the superior reversible redox reactions and excellent supercapacitive characteristic of amorphous porous Mn_3O_4/NGP electrodes. The areal C_{sp} measured for amorphous porous Mn_3O_4/NGP

DOI: 10.1021/acsami.5b02157
ACS Appl. Mater. Interfaces 2015, 7, 11444−11451

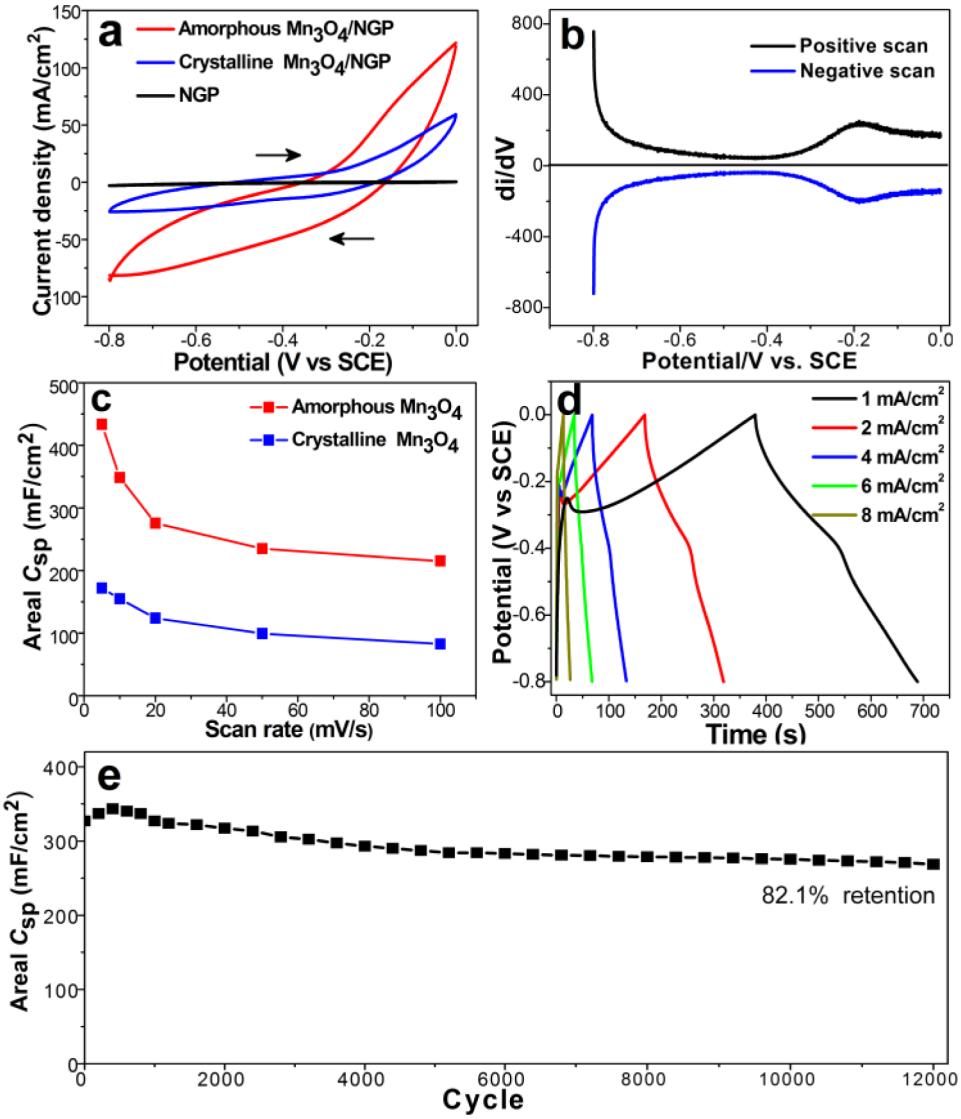

Figure 3. (a) CVs of amorphous porous Mn_3O_4/NGP, crystalline Mn_3O_4/NGP, and NGP electrodes at 100 mV/s; (b) di/dV−potential curves of amorphous porous Mn_3O_4/NGP; (c) areal capacitance and capacitance retention of amorphous porous Mn_3O_4/NGP and crystalline Mn_3O_4/NGP electrodes as a function of scan rate; (d) galvanostatic charge−discharge curves of amorphous porous Mn_3O_4/NGP electrode at different current densities of 1−8 mA/cm^2; and (e) cycling performance of amorphous porous Mn_3O_4/NGP electrode.

electrode at 1.0 mA/cm^2 is 372.5 mF/cm^2 (372.5 F/g). The summary plot of C_{sp} versus current density is shown in Supporting Information Figure S4, which also demonstrates the amorphous porous Mn_3O_4/NGP electrode exhibits much enhanced supercapacitive performance compared with the crystalline Mn_3O_4/NGP electrodes. The long-term cycling performance of amorphous porous Mn_3O_4/NGP electrode was evaluated at a high scan rate of 100 mV/s for 12 000 cycles. As shown in Figure 3e, the amorphous porous Mn_3O_4/NGP electrode exhibits a high retention of the initial C_{sp} (82.1%) at a high scan rate of 100 mV/s after 12 000 cycles. The relationship between electrode performance and deposition time of Mn_3O_4 was also studied. When the deposition time is 30 min, the amorphous porous Mn_3O_4/NGP electrode exhibits the highest C_{sp} as shown in Supporting Information Figure S5.

In order to fabricate well a complete asymmetric electronic device, the positive electrode is also very important. So we fabricate a kind of amorphous $Ni(OH)_2$/NGP via electrochemical oxidation of NGP. The experiment procedure of fabricating $Ni(OH)_2$/NGP electrodes was shown in the Supporting Information. The characterizations of amorphous $Ni(OH)_2$/NGP electrodes were carried out, and the results are shown in Figures S9−18 in Supporting Information. The amorphous $Ni(OH)_2$/NGP electrode exhibits a high areal C_{sp} (1646 mF/cm^2 at 5 mV/s) and superior cycling stability (82.5% retention of the initial areal C_{sp} at a high scan rate of 100 mV/s after 12 000 cycles). The amorphous porous $Ni(OH)_2$ exhibits a BET surface area of about 51.75 m^2/g, and the relative details are shown in Supporting Information Figure S23.

The asymmetric paper-based supercapacitor was assembled using an amorphous porous Mn_3O_4/NGP as negative electrode and a $Ni(OH)_2$/NGP as positive electrode as shown in Figure 4a. The PVA/NaOH gel was utilized as solid−gel electrolyte. On the basis of the amorphous porous Mn_3O_4/NGP as negative electrode and amorphous $Ni(OH)_2$/NGP as positive electrode, the assembled Mn_3O_4//$Ni(OH)_2$-APSC devices are planar and thin (0.4 mm) and have excellent flexibility as shown in Figure 4c−e. CVs of the Mn_3O_4//$Ni(OH)_2$-APSCs device at

DOI: 10.1021/acsami.5b02157
ACS Appl. Mater. Interfaces 2015, 7, 11444−11451

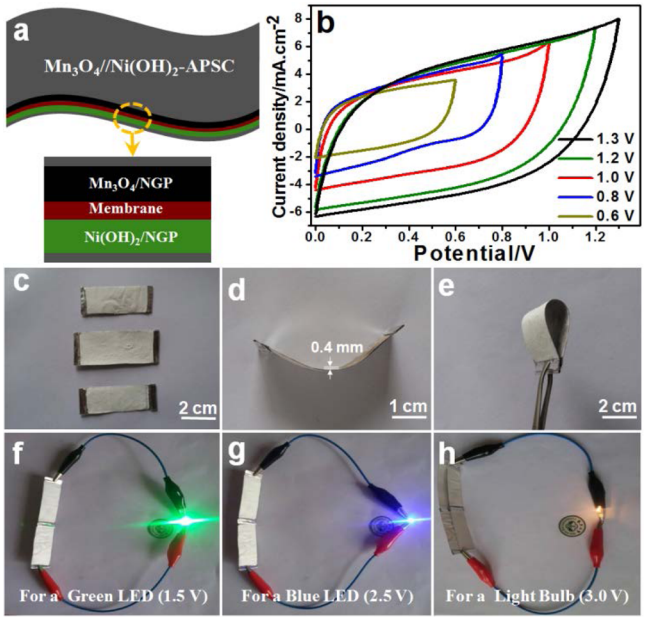

Figure 4. (a) Schematic illustration for the assembled Mn_3O_4//$Ni(OH)_2$-APSC devices and (b) CVs of the APSC device under various electrochemical windows at 50 mV/s. The assembled APSCs: (c) normal state, (d–e) bending states, (f) a green LED powered by 2 ATFSCs in series, (g) a blue LED powered by 2 ATFSCs in series, and (h) a light bulb powered by 4 ATFSCs in series and parallel.

different voltage windows at 50 mV/s are shown in Figure 4b, which shows the voltage window can be extended to 1.3 V. This is also supported by the galvanostatic charge/discharge measurements as shown in Supporting Information Figure S19. The good symmetries of charge/discharge curves confirm good capacitive behavior of the assembled Mn_3O_4//$Ni(OH)_2$-APSCs device. When the operation potential increased from 0.6 to 1.3 V at 50 mV/s, the volumetric C_{sp} is increased from 0.71 to 1.96 F/cm^3, with an enhancement of more than 270%. To further demonstrate the practical application of Mn_3O_4//$Ni(OH)_2$-APSCs, two devices are connected in series to power a green light-emitting (LED, working voltage: 1.5 V) for 10 min after being charged at 4.0 mA/cm^2 for 60 s as shown in Figure 4f. Two Mn_3O_4// $Ni(OH)_2$-APSC devices connected in series can power a blue LED (working voltage: 2.5 V) for 10 min after being charged at current density of 4.0 mA/cm^2 for 90 s as shown in Figure 4g. Four Mn_3O_4//$Ni(OH)_2$-APSCs connected in series and in parallel can power a light bulb (working voltage: 3.0 V) for 280 s after being charged at 4.0 mA/cm^2 for 120 s as shown in Figure 4h. Therefore, the above results demonstrated that the low-cost APSCs will be a kind of promising flexible and lightweight power supply devices.

To further study the performance of the device, CVs of Mn_3O_4//$Ni(OH)_2$-APSCs at different scan rates are measured, and they all have rectangular-like shapes as shown in Figure 5a, which shows the ideal capacitive behavior and fast charge/discharge properties of the assembled Mn_3O_4//$Ni(OH)_2$-APSCs. The volumetric C_{sp} of Mn_3O_4//$Ni(OH)_2$-APSCs at 10 mV/s is 3.05 F/cm^3, which is much larger than those of many reported all-solid-state SCs, such as graphene-SSCs (0.42 F/cm^3),[48] TiN-SSCs (0.33 F/cm^3),[49] ZnO@MnO_2-SSCs (0.33 F/cm^3),[50] ZnO@MnO_2//graphene-ASCs (0.52 F/cm^3),[51] MnO_2//Fe_2O_3-ASCs (1.21 F/cm^3),[28] and MnO_2 planar SSCs (0.48 F/cm^3).[36] The dependence of volumetric C_{sp} on scan rate is shown in Supporting Information Figure S20, which shows that the Mn_3O_4//$Ni(OH)_2$-APSCs have a good rate capability of 57% when the scan rate increases from 5 to 100 mV/s. Additionally, the triangular shapes of charge/discharge curves at different current densities further confirm high electrochemical properties of Mn_3O_4//$Ni(OH)_2$-APSCs as shown in Figure 5b. The Mn_3O_4//$Ni(OH)_2$-APSCs at 1.0 mA/cm^2 also exhibits a large volumetric C_{sp} of 2.07 F/cm^3, which is substantially larger than those obtained from many all-solid-state symmetric SCs (SSCs)[52−54] and ASCs.[55−57] The Mn_3O_4//$Ni(OH)_2$-APSCs exhibit excellent mechanical flexibility, and the different bending states almost do not affect their electrochemical performance as shown in Figure 5c, indicating high potential for the applications in flexible energy storage devices.

Figure 5d shows the Ragone plot of the Mn_3O_4//$Ni(OH)_2$-APSCs calculated from galvanostatic discharge curves. The APSCs exhibit a high volumetric energy density of 0.35 mW h/cm^3 at a current density of 0.5 mA/cm^2, and this remains 0.30 mW h/cm^3 at 1.0 mA/cm^2, confirming high rate performance of the Mn_3O_4//$Ni(OH)_2$-APSC device. Furthermore, the achieved maximum volumetric energy density is considerably higher than those of recently reported all-solid-state SSCs and ASCs such as ZnO@MnO_2//graphene-ASCs (0.234 mW h/cm^3),[57] carbon nanotube (CNT)/$Ni(OH)_2$-ASCs (0.30 mW h/cm^3),[58,59] single-walled carbon nanotubes-based (SCNTs)-SSCs (0.01 mWh/cm^3),[60,61] graphite/paper-SSCs (<0.10 mW h/cm^3),[62,63] TiO_2@PPy-SSCs (0.013 mW h/cm^3),[64] and TiO_2@C-SSCs (0.011 mW h/cm^3).[65] Additionally, the Mn_3O_4//$Ni(OH)_2$-ASC device can deliver a high power density of 32.5 mW/cm^3 at 5 mA/cm^2, which is much higher than those of ZnO@MnO_2-SSCs,[56] ZnO@MnO_2// graphene ASCs,[57] and graphite/paper-SSCs.[62] The energy and power density of Mn_3O_4//$Ni(OH)_2$-APSCs are also higher or comparable to some liquid systems such as PANI//WO_x@MnO_2-ASCs (0.002 mW h/cm^3 and 0.009 mW/cm^3),[59] cotton-graphene SSCs (18 Wh/kg, 1.2 kW/kg),[61] and 3D-MnO_2 SCs (10.4 Wh/kg, 14.7 kW/kg).[63] The long-term cycling stability of Mn_3O_4//$Ni(OH)_2$-APSCs was also tested at a high scan rate of 100 mV/s for 12 000 cycles. As shown in Figure 5e, this ASC device exhibits 83.3% retention of the initial C_{sp} at 100 mV/s after 12 000 cycles, revealing its high cycling stability. The above results confirm that the amorphous porous Mn_3O_4/NGP is promising as a high-performance negative-electrode for APSCs.

4. CONCLUSIONS

In summary, the novel paper-based SCs, Mn_3O_4//$Ni(OH)_2$-APSCs, were successfully fabricated, and they provided a high areal C_{sp} of 3.05 F/cm^3 at 5 mV/s and superior cycling stability. The paper-based asymmetric supercapacitor also achieved a maximum energy density of 0.35 mW h/cm^3 at 0.5 mA/cm^2 and a maximum power density of 32.5 mW/cm^3 at 5 mA/cm^2, which are substantially higher than those of most reported all-solid-state SSCs and ASCs. The device exhibits superior cycling performance (<17% C_{sp} loss after 12 000 cycles at a high scan rate of 100 mV/s). Additionally, the new kind of negative material we fabricated, amorphous porous Mn_3O_4, exhibits 432 mF/cm^2 capacitance at 5 mV/s and superior cycling stability. This work shows an important breakthrough in the design and fabrication of APSCs with high energy/power densities and superior cycling stability and amorphous porous metal oxide/NGP electrodes for the high-performance SCs.

DOI: 10.1021/acsami.5b02157
ACS Appl. Mater. Interfaces 2015, 7, 11444−11451

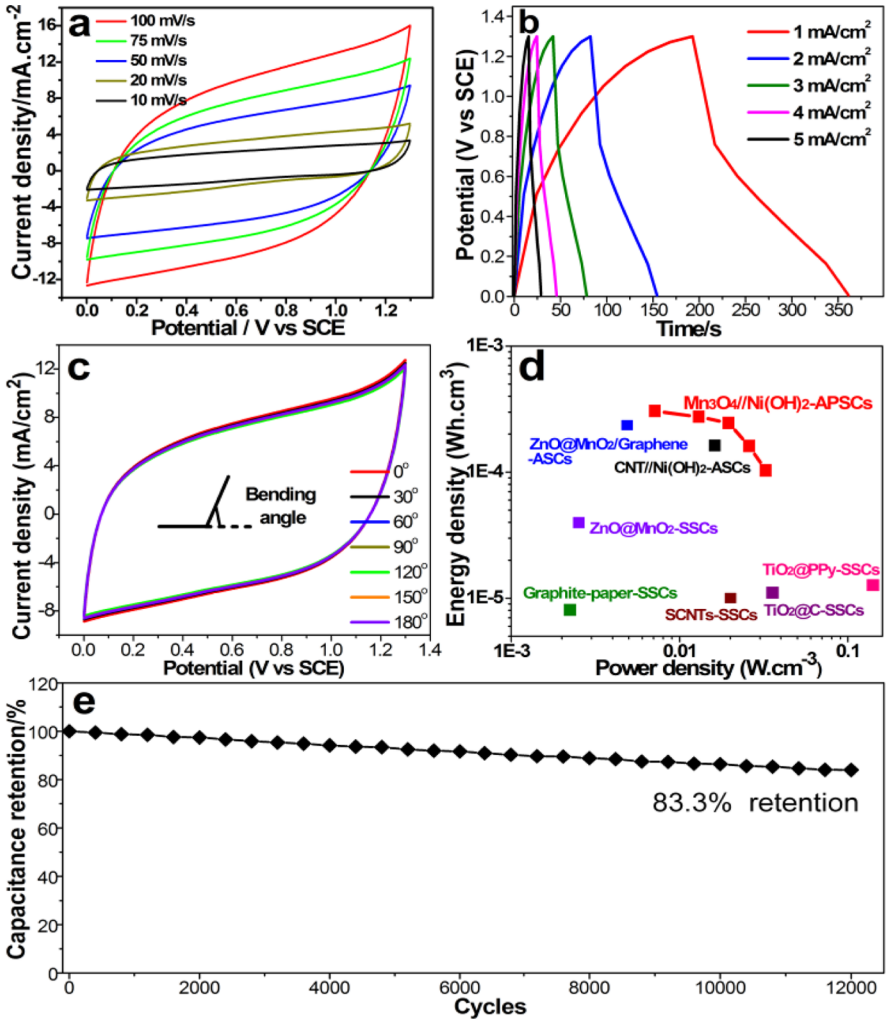

Figure 5. (a) CVs of Mn_3O_4//$Ni(OH)_2$-APSC at 100 mV/s, (b) galvanostatic charge−discharge curves of Mn_3O_4//$Ni(OH)_2$-APSC at different current densities of 1−5 mA/cm^2, (c) CVs of the APSC device under various bending states at 75 mV/s, (d) Ragone plots of the APSC devices. The maximum volumetric energy densities and power densities reported for the other all-solid-state SSCs and ASCs are added for comparison.[45−50] (e) Cycling performance of the Mn_3O_4//$Ni(OH)_2$-APSC.

■ ASSOCIATED CONTENT

Supporting Information

NGP fabricatation process; CV and galvanostatic data from amorphous Mn_3O_4/NGP; SEM, XRD characterization, and electrochemical data for crystalline Mn_3O_4; XPS, XRD, and electrochemical data for $Ni(OH)_2$/NGP positive electrode; and BET curves for Mn_3O_4 and $Ni(OH)_2$. The Supporting Information is available free of charge on the ACS Publications website at DOI: 10.1021/acsami.5b02157.

■ AUTHOR INFORMATION

Corresponding Author

*E-mail: ligaoren@mail.sysu.edu.cn. Fax: 86-20-84112245. Phone: 86-20-84110071.

Notes

The authors declare no competing financial interest.

■ ACKNOWLEDGMENTS

This work was supported by NSFC (51173212 and J1103305), Natural Science Foundation of Guangdong Province (S2013020012833), Fundamental Research Fund for the Central Universities (13lgpy51), SRF for ROCS, SEM ([2012]1707), the Project of High Level Talents in Higher School of Guangdong Province, and Open-End Fund of Key Laboratory of Functional Inorganic Material Chemistry (Heilongjiang University), Ministry of Education.

■ REFERENCES

(1) Yang, Y.; Ruan, G.; Xiang, C.; Wang, G.; Tour, J. M. Flexible Three-dimensional Nanoporous Metal-based Energy Devices. *J. Am. Chem. Soc.* **2014**, *136*, 6187−6190.

(2) Peng, L.; Peng, X.; Liu, B.; Wu, C.; Xie, Y.; Yu, G. Ultrathin Two-dimensional MnO_2/graphene Hybrid Nanostructures for High-performance, Flexible Planar Supercapacitors. *Nano Lett.* **2013**, *13*, 2151−2157.

(3) Cheng, Y.; Lu, S.; Zhang, H.; Varanasi, C. V.; Liu, J. Synergistic Effects from Graphene and Carbon Nanotubes Enable Flexible and Robust Electrodes for High-Performance Supercapacitors. *Nano Lett.* **2012**, *12*, 4206−4211.

(4) Nyholm, L.; Nyström, G.; Mihranyan, A.; Strømme, M. Toward Flexible Polymer and Paper-Based Energy Storage Devices. *Adv. Mater.* **2011**, *23*, 3751−3769.

(5) Kim, S.-K.; Koo, H.-J.; Lee, A.; Braun, P. V. Selective Wetting-Induced Micro-Electrode Patterning for Flexible Micro-Supercapacitors. *Adv. Mater.* **2014**, *26*, 5108−5112.

DOI: 10.1021/acsami.5b02157
ACS Appl. Mater. Interfaces 2015, 7, 11444−11451

(6) Liu, L.; Niu, Z.; Zhang, L.; Zhou, W.; Chen, X.; Xie, S. Nanostructured Graphene Composite Papers for Highly Flexible and Foldable Supercapacitors. *Adv. Mater.* **2014**, *26*, 4855−4862.
(7) Dong, X.; Guo, Z.; Song, Y.; Hou, M.; Wang, J.; Wang, Y.; Xia, Y. Flexible and Wire-Shaped Micro-Supercapacitor Based on $Ni(OH)_2$-Nanowire and Ordered Mesoporous Carbon Electrodes. *Adv. Funct. Mater.* **2014**, *24*, 3405−3412.
(8) Zhao, J.; Chen, J.; Xu, S.; Shao, M.; Zhang, Q.; Wei, F.; Ma, J.; Wei, M.; Evans, D. G.; Duan, X. Hierarchical NiMn Layered Double Hydroxide/Carbon Nanotubes Architecture with Superb Energy Density for Flexible Supercapacitors. *Adv. Funct. Mater.* **2014**, *24*, 2938−2946.
(9) Shen, L.; Che, Q.; Li, H.; Zhang, X. Mesoporous $NiCo_2O_4$ Nanowire Arrays Grown on Carbon Textiles as Binder-Free Flexible Electrodes for Energy Storage. *Adv. Funct. Mater.* **2014**, *24*, 2630−2637.
(10) Choi, C.; Lee, J. A.; Choi, A. Y.; Kim, Y. T.; Lepró, X.; Lima, M. D.; Baughman, R. H.; Kim, S. J. Flexible Supercapacitor Made of Carbon nanotube yarn with internal pores. *Adv. Mater.* **2014**, *26*, 2059−2065.
(11) Wang, X.; Lu, X.; Liu, B.; Chen, D.; Tong, Y.; Shen, G. Flexible Energy-Storage Devices: Design Consideration and Recent Progress. *Adv. Mater.* **2014**, *26*, 4763−4782.
(12) Xiao, X.; Peng, X.; Jin, H.; Li, T.; Zhang, C.; Gao, B.; Hu, B.; Huo, K.; Zhou, J. Freestanding Mesoporous VN/CNT Hybrid Electrodes for Flexible All-Solid-State Supercapacitors. *Adv. Mater.* **2013**, *25*, 5091−5097.
(13) Zhang, F.; Yuan, C.; Zhu, J.; Wang, J.; Zhang, X.; Lou, X. W. Flexible Films Derived from Electrospun Carbon Nanofibers Incorporated with Co_3O_4 Hollow Nanoparticles as Self-Supported Electrodes for Electrochemical Capacitors. *Adv. Funct. Mater.* **2013**, *23*, 3909−3915.
(14) Niu, Z.; Zhang, L.; Liu, L.; Zhu, B.; Dong, H.; Chen, X. All-Solid-State Flexible Ultrathin Micro-Supercapacitors Based on Graphene. *Adv. Mater.* **2013**, *25*, 4035−4042.
(15) Yuan, L.; Xiao, X.; Ding, T.; Zhong, J.; Zhang, X.; Shen, Y.; Hu, B.; Huang, Y.; Zhou, J.; Wang, Z. L. Paper-Based Supercapacitors for Self-Powered Nanosystems. *Angew. Chem., Int. Ed.* **2012**, *51*, 5018−5022.
(16) Li, S.; Huang, D.; Zhang, B.; Xu, X.; Wang, M.; Yang, G.; Shen, Y. Recent Advances in Design and Fabrication of Electrochemical Supercapacitors with High Energy Densities. *Adv. Energy. Mater.* **2014**, *4*, 1470050−14700054.
(17) Hu, L.; Cui, Y. Energy and Environmental Nanotechnology in Conductive Paper and Textiles. *Energy Environ. Sci.* **2012**, *5*, 6423−6435.
(18) Kaempgen, M.; Chan, C.; Ma, J.; Cui, Y.; Gruner, G. Printable Thin Film Supercapacitors Using Single-walled Carbon Nanotubes. *Nano Lett.* **2009**, *9*, 1872−1876.
(19) Zheng, G.; Hu, L.; Wu, H.; Xie, X.; Cui, Y. Paper Supercapacitors by a Solvent-free Drawing Method. *Energy Environ. Sci.* **2011**, *4*, 3368−3373.
(20) Xu, J.; Wang, Q.; Wang, X.; Xiang, Q.; Liang, B.; Chen, D.; Shen, G. Flexible Asymmetric Supercapacitors Based Upon Co_9S_8 Nanorod//Co_3O_4@RuO_2 Nanosheet Arrays on Carbon Cloth. *ACS Nano* **2013**, *7*, 5453−5462.
(21) Yang, P.; Ding, Y.; Lin, Z.; Chen, Z.; Li, Y.; Qiang, P.; Ebrahimi, M.; Mai, W.; Wong, C.; Wang, Z. L. Low-cost high-performance solid-state asymmetric supercapacitors based on MnO_2 nanowires and Fe_2O_3 nanotubes. *Nano Lett.* **2014**, *14*, 731−736.
(22) Wang, X.; Liu, B.; Liu, R.; Wang, Q.; Hou, X.; Chen, D.; Wang, R.; Shen, G. Fiber-Based Flexible All-Solid-State Asymmetric Supercapacitors for Integrated Photodetecting System. *Angew. Chem., Int. Ed.* **2014**, *53*, 1880−1884.
(23) Chen, L.; Huang, Z.; Liang, H.; Guan, Q.; Yu, S. Supercapacitors: Bacterial-Cellulose-Derived Carbon Nanofiber@MnO_2 and Nitrogen-Doped Carbon Nanofiber Electrode Materials: An Asymmetric Supercapacitor with High Energy and Power Density. *Adv. Mater.* **2013**, *25*, 4816−4821.
(24) Zhu, J.; Cao, L.; Wu, Y.; Gong, Y.; Liu, Z.; Hoster, H. E.; Zhang, Y.; Zhang, S.; Yang, S.; Yan, Q.; Ajayan, P. M.; Vajtai, R. Building 3D Structures of Vanadium Pentoxide Nanosheets and Application as Electrodes in Supercapacitors. *Nano Lett.* **2013**, *13*, 5408−5413.
(25) Cheng, Y.; Lu, S.; Zhang, H.; Varanasi, C. V.; Liu, J. Synergistic Effects from Graphene and Carbon Nanotubes Enable Flexible and Robust Electrodes for High-performance Supercapacitors. *Nano Lett.* **2012**, *12*, 4206−4211.
(26) Wang, B.; Chen, J. S.; Wang, Z.; Madhavi, S.; Lou, X. W. Green Synthesis of NiO Nanobelts with Exceptional Pseudo-capacitive Properties. *Adv. Energy Mater.* **2012**, *2*, 1188−1192.
(27) Hu, C.; Chang, K.; Lin, M.; Wu, Y. Design and Tailoring of the Nanotubular Arrayed Architecture of Hydrous RuO_2 for Next Generation Supercapacitors. *Nano Lett.* **2006**, *6*, 2690−2695.
(28) Lu, X.; Zeng, Y.; Yu, M.; Zhai, T.; Liang, C.; Xie, S.; Balogun, M. S.; Tong, Y. Oxygen-Deficient Hematite Nanorods as High-Performance and Novel Negative Electrodes for Flexible Asymmetric Supercapacitors. *Adv. Mater.* **2014**, *26*, 3148−3155.
(29) Masarapu, C.; Zeng, H. F.; Hung, K. H.; Wei, B. Effect of Temperature on the Capacitance of Carbon Nanotube Supercapacitors. *ACS Nano* **2009**, *3*, 2199−2206.
(30) Zhang, D.; Miao, M.; Niu, H.; Wei, Z. Core-spun Carbon Nanotube Yarn Supercapacitors for Wearable Electronic Textiles. *ACS Nano* **2014**, *8*, 4571−4579.
(31) Choi, B. G.; Yang, M.; Hong, W. H.; Choi, J. W.; Huh, Y. S. 3D Macroporous Graphene Frameworks for Supercapacitors with High Energy and Power Densities. *ACS Nano* **2012**, *6*, 4020−4028.
(32) Chang, J.; Jin, M.; Yao, F.; Kim, T.; Le, V.; Yue, H.; Gunes, F.; Li, B.; Ghosh, A.; Xie, S.; Lee, Y. Asymmetric Supercapacitors Based on Graphene/MnO_2 Nanospheres and Graphene/MoO_3 Nanosheets with High Energy Density. *Adv. Funct. Mater.* **2013**, *23*, 5074−5083.
(33) Xu, J.; Wang, Q.; Wang, X.; Xiang, Q.; Hang, B.; Chen, D.; Shen, G. Flexible Asymmetric Supercapacitors Based upon Co_9S_8 Nanorod//Co_3O_4@RuO_2 Nanosheet Arrays on Carbon Cloth. *ACS Nano* **2013**, *7*, 5453−5462.
(34) Yu, G.; Hu, L.; Vosgueritchian, M.; Wang, H.; Xie, X.; McDonough, J. R.; Cui, X.; Cui, Y.; Bao, Z. Solution-processed Graphene/MnO_2 Nanostructured Textiles for High-performance Electrochemical Capacitors. *Nano Lett.* **2011**, *11*, 2905−2911.
(35) Feng, J.; Li, Q.; Lu, X.; Tong, Y.; Li, G. Flexible Symmetrical Planar Supercapacitors Based on Multi-layered MnO_2/Ni/graphite/paper Electrodes with High-efficient Electrochemical Energy Storage. *J. Mater. Chem. A* **2014**, *2*, 2985−2992.
(36) Feng, J.; Ye, S.; Wang, A.; Lu, X.; Tong, Y.; Li, G. Flexible Cellulose Paper-based Asymmetrical Thin Film Supercapacitors with High-Performance for Electrochemical Energy Storage. *Adv. Funct. Mater.* **2014**, *24*, 7093−7101.
(37) Zhou, C.; Zhang, Y.; Li, Y.; Liu, J. Construction of High Capacitance 3D CoO@Polypyrrole Nanowire Array Electrode for Aqueous Asymmetric Supercapacitor. *Nano Lett.* **2013**, *13*, 2078−2085.
(38) Xiao, X.; Ding, T.; Yuan, L.; Shen, Y.; Zhong, Q.; Zhang, X.; Cao, Y.; Hu, B.; Zhai, T.; Gong, L.; Chen, J.; Tong, Y.; Zhou, J.; Wang, Z. L. WO_{3-x}/MoO_{3-x} Core/Shell Nanowires on Carbon Fabric as an Anode for All-Solid-State Asymmetric Supercapacitors. *Adv. Energy Mater.* **2012**, *2*, 1328−1332.
(39) Jin, W. H.; Cao, G. T.; Sun, J. Y. Biomolecule-assisted Synthesis of Cobalt Sulfide Nanowires for Application in Supercapacitors. *J. Power Sources* **2008**, *175*, 676−681.
(40) Qu, Q. T.; Yang, S. B.; Feng, X. L. 2D Sandwich-like Sheets of Iron Oxide Grown on Graphene as High Energy Anode Material for Supercapacitors. *Adv. Mater.* **2011**, *23*, 5574−5580.
(41) Bao, L.; Li, X. Towards Textile Energy Storage from Cotton T-shirts. *Adv. Mater.* **2012**, *24*, 3246−3252.
(42) Pietrzak, R.; Jurewicz, K.; Nowicki, P.; Babel, K.; Wachowska, H. Microporous Activated Carbons from Ammoxidised Anthracite and Their Capacitance Behaviours. *Fuel* **2007**, *86*, 1086−1092.
(43) Wu, Z.; Winter, A.; Chen, L.; Sun, Y.; Turchanin, A.; Feng, X.; Müllen, K. Three-Dimensional Nitrogen and Boron Co-doped

DOI: 10.1021/acsami.5b02157
ACS Appl. Mater. Interfaces 2015, 7, 11444−11451

Graphene for High-Performance All-Solid-State Supercapacitors. *Adv. Mater.* **2012**, *24*, 5130−5135.
(44) Guo, C.; Chitre, A.; Lu, X. DNA-assisted Assembly of Carbon Nanotubes and MnO_2 Nanospheres as Electrodes for High-performance Asymmetric Supercapacitors. *Phys. Chem. Chem. Phys.* **2014**, *16*, 4672−4678.
(45) (a) Lee, K.; Deng, S.; Fan, H.; Mhaisalkar, S.; Tan, H.; Tok, E.; Loh, K.; Chin, W.; Sow, C. α-Fe_2O_3 Nanotubes-reduced Graphene Oxide Composites as Synergistic Electrochemical Capacitor Materials. *Nanoscale* **2012**, *4*, 2958−2961.
(46) Binitha, G.; Soumya, M.; Madhavan, A.; Praveen, P.; Balakrishnan, A.; Subramanian, K.; Reddy, M.; Nair, S.; Nair, A.; Sivakumar, N. Electrospun α-Fe_2O_3 Nanostructures for Supercapacitor Applications. *J. Mater. Chem. A* **2013**, *1*, 11698−11704.
(47) Mendoza-Sánchez, B.; Brousse, T.; Ramirez-Castro, C.; Nicolosi, V.; Grant, P. An Investigation of Nanostructured Thin Film α-MoO_3 Based Supercapacitor Electrodes in An Aqueous Electrolyte. *Electrochim. Acta* **2013**, *91*, 253−260.
(48) Simon, P.; Gogotsi, Y. Materials for Electrochemical Capacitors. *Nat. Mater.* **2008**, *7*, 845−854.
(49) Lu, X.; Wang, G.; Zhai, T.; Yu, M.; Xie, S.; Ling, Y.; Liang, C.; Tong, Y.; Li, Y. Stabilized TiN Nanowire Arrays for High-performance and Flexible Supercapacitors. *Nano Lett.* **2012**, *12*, 5376−5381.
(50) Yang, P.; Xiao, X.; Li, Y.; Ding, Y.; Qiang, P.; Tan, X.; Mai, W.; Lin, Z.; Wu, W.; Li, T.; Jin, H.; Liu, P.; Zhou, J.; Wong, C.; Wang, Z. L. Hydrogenated ZnO Core−shell Nanocables for Flexible Supercapacitors and Self-powered Systems. *ACS Nano* **2013**, *7*, 2617−2626.
(51) Wang, Z.; Zhu, Z.; Qiu, J.; Yang, S. High Performance Flexible Solid-state Asymmetric Supercapacitors from MnO_2/ZnO Core−shell Nanorods Specially Reduced Graphene Oxide. *J. Mater. Chem. C* **2014**, *2*, 1331−1336.
(52) Qin, Y.; Wang, X.; Wang, Z. Microfibre-nanowire Hybrid Structure for Energy Scavenging. *Nature* **2008**, *451*, 809−813.
(53) Hu, L. B.; Choi, J. W.; Yang, Y.; Jeong, S.; La Mantia, F.; Cui, L. F.; Cui, Y. Highly Conductive Paper for Energy-storage Devices. *Proc. Natl. Acad. Sci. U.S.A.* **2009**, *106*, 21490−21494.
(54) Tobjork, D.; Osterbacka, R. Paper Electronics. *Adv. Mater.* **2011**, *23*, 1935−1961.
(55) Yuan, L.; Yao, B.; Hu, B.; Huo, K.; Chen, W.; Zhou, J. Polypyrrole-coated Paper for Flexible Solid-state Energy Storage. *Energy Environ. Sci.* **2013**, *6*, 470−476.
(56) Nyström, G.; Razaq, A.; Strømme, M.; Nyholm, L.; Mihranyan, A. Ultrafast All-polymer Paper-based Batteries. *Nano Lett.* **2009**, *9*, 3635−3639.
(57) Chigane, M.; Ishikawa, M. Manganese Oxide Thin Film Preparation by Potentiostatic Electrolyses and Electrochromism. *J. Electrochem. Soc.* **2000**, *147*, 2246−2251.
(58) Tang, Z.; Tang, C. H.; Gong, H. A High Energy Density Asymmetric Supercapacitor from Nano-architectured $Ni(OH)_2$/Carbon Nanotube Electrodes. *Adv. Funct. Mater.* **2012**, *2*, 1272−1278.
(59) Xiao, X.; Peng, X.; Jin, H.; Li, T.; Zhang, C.; Gao, B.; Hu, B.; Huo, K.; Zhou, J. Freestanding Mesoporous VN/CNT Hybrid Electrodes for Flexible All-Solid-State Supercapacitors. *Adv. Mater.* **2013**, *25*, 5091−5097.
(60) Kaempgen, M.; Chan, C.; Ma, J.; Cui, Y.; Gruner, G. Printable thin film supercapacitors using single-walled carbon nanotubes. *Nano Lett.* **2009**, *9*, 1872−1876.
(61) Liu, W.; Yan, X.; Lang, J.; Peng, C.; Xue, Q. Flexible and Conductive nanocomposite electrode based on graphene sheets and cotton cloth for supercapacitor. *J. Mater. Chem.* **2012**, *22*, 17245−17253.
(62) Zheng, G.; Hu, L.; Wu, H.; Xie, X.; Cui, Y. Paper supercapacitors by a solvent-free drawing method. *Energy Environ. Sci.* **2011**, *4*, 3368−3373.
(63) Wang, Y.; Lu, A.; Zhang, H.; Li, W. Synthesis of Nanostructured Mesoporous Manganese Oxides with Three-Dimensional Frameworks and Their Application in Supercapacitors. *J. Phys. Chem. C* **2011**, *115*, 5413−5421.
(64) Yu, M.; Zeng, Y.; Zhang, C.; Lu, X.; Zeng, C.; Yao, C.; Yang, Y.; Tong, Y. Titanium Dioxide@Polypyrrole Core-shell Nanowires for All Solid-state Flexible Supercapacitors. *Nanoscale* **2013**, *5*, 10806−10810.
(65) Zheng, H.; Zhai, T.; Yu, M.; Xie, S.; Liang, C.; Zhao, W.; Wang, S.; Zhang, Z.; Lu, X. TiO_2@C Core-shell Nanowires for High-performance and Flexible Solid-state Supercapacitors. *J. Mater. Chem. C* **2013**, *1*, 225−229.

DOI: 10.1021/acsami.5b02157
ACS Appl. Mater. Interfaces 2015, 7, 11444−11451